Downloaded from orbit.dtu.dk on: Dec 20, 2017

Technical University of Denmark

# Influence of helium puff on divertor asymmetry in experimental advanced superconducting tokamak

**Liu, S. C.; Guo, H. Y.; Xu, G. S.; Wang, L.; Wang, H. Q.; Ding, R.; Duan, Y. M.; Gan, K. F.; Shao, L. M.; Chen, L.; Yan, Ning; Zhang, W.; Chen, R.; Xiong, H.; Ding, S.; Hu, G. H.; Liu, Y. L.; Zhao, N.; Li, Y. L.; Gao, X.**

*Published in:*
Physics of Plasmas

*Link to article, DOI:*
10.1063/1.4863843

*Publication date:*
2014

*Document Version*
Publisher's PDF, also known as Version of record

Link back to DTU Orbit

*Citation (APA):*
Liu, S. C., Guo, H. Y., Xu, G. S., Wang, L., Wang, H. Q., Ding, R., ... Gao, X. (2014). Influence of helium puff on divertor asymmetry in experimental advanced superconducting tokamak. Physics of Plasmas, 21(2), [022509]. DOI: 10.1063/1.4863843

DTU Library
Technical Information Center of Denmark

**General rights**
Copyright and moral rights for the publications made accessible in the public portal are retained by the authors and/or other copyright owners and it is a condition of accessing publications that users recognise and abide by the legal requirements associated with these rights.

- Users may download and print one copy of any publication from the public portal for the purpose of private study or research.
- You may not further distribute the material or use it for any profit-making activity or commercial gain
- You may freely distribute the URL identifying the publication in the public portal

If you believe that this document breaches copyright please contact us providing details, and we will remove access to the work immediately and investigate your claim.


# Influence of helium puff on divertor asymmetry in Experimental Advanced Superconducting Tokamak

S. C. Liu, H. Y. Guo, G. S. Xu, L. Wang, H. Q. Wang, R. Ding, Y. M. Duan, K. F. Gan, L. M. Shao, L. Chen, N. Yan, W. Zhang, R. Chen, H. Xiong, S. Ding, G. H. Hu, Y. L. Liu, N. Zhao, Y. L. Li, and X. Gao

Citation: Physics of Plasmas (1994-present) **21**, 022509 (2014); doi: 10.1063/1.4863843
View online: http://dx.doi.org/10.1063/1.4863843
View Table of Contents: http://scitation.aip.org/content/aip/journal/pop/21/2?ver=pdfcov
Published by the AIP Publishing

**Articles you may be interested in**

Conceptual design of a divertor Thomson scattering diagnostic for NSTX-Ua)
Rev. Sci. Instrum. **85**, 11E825 (2014); 10.1063/1.4894001

Recent advances in long-pulse high-confinement plasma operations in Experimental Advanced Superconducting Tokamaka)
Phys. Plasmas **21**, 056107 (2014); 10.1063/1.4872195

Experimental investigation of density behaviors in front of the lower hybrid launcher in experimental advanced superconducting tokamak
Phys. Plasmas **20**, 062507 (2013); 10.1063/1.4812462

Divertor asymmetry and scrape-off layer flow in various divertor configurations in Experimental Advanced Superconducting Tokamak
Phys. Plasmas **19**, 042505 (2012); 10.1063/1.4707396

Biasing, acquisition, and interpretation of a dense Langmuir probe array in NSTXa)
Rev. Sci. Instrum. **81**, 10E130 (2010); 10.1063/1.3490025


This article is copyrighted as indicated in the article. Reuse of AIP content is subject to the terms at: http://scitation.aip.org/termsconditions. Downloaded to IP: 192.38.67.112 On: Thu, 25 Dec 2014 10:55:46

# Influence of helium puff on divertor asymmetry in Experimental Advanced Superconducting Tokamak

S. C. Liu,[1,a)] H. Y. Guo,[1,2] G. S. Xu,[1] L. Wang,[1,3] H. Q. Wang,[1] R. Ding,[1] Y. M. Duan,[1] K. F. Gan,[1] L. M. Shao,[1] L. Chen,[1] N. Yan,[1,4] W. Zhang,[1] R. Chen,[1] H. Xiong,[1] S. Ding,[1] G. H. Hu,[1] Y. L. Liu,[1] N. Zhao,[1] Y. L. Li,[1] and X. Gao[1]
[1]*Institute of Plasma Physics, Chinese Academy of Sciences, Hefei 230031, China*
[2]*Tri Alpha Energy, Inc., Post Office Box 7010, Rancho Santa Margarita, California 92688, USA*
[3]*School of Physics and Optoelectronic Technology, Dalian university of Technology, Dalian 116024, China*
[4]*Association Euratom-Risø DTU, DK-4000 Roskilde, Denmark*

(Received 5 June 2013; accepted 16 January 2014; published online 21 February 2014)

Divertor asymmetries with helium puffing are investigated in various divertor configurations on Experimental Advanced Superconducting Tokamak (EAST). The outer divertor electron temperature decreases significantly during the gas injection at the outer midplane. As soon as the gas is injected into the edge plasma, the power deposition drops sharply at the lower outer target while increases gradually at the lower inner target in LSN configuration; the power deposition increases quickly at the upper outer target while remains unchanged at the upper inner target in upper single null configuration; the power deposition increases slightly at the outer targets while shows no obvious variation at the inner targets in double null configuration. The radiated power measured by the extreme ultraviolet arrays increases significantly due to helium gas injection, especially in the outer divertor. The edge parameters are measured by reciprocating probes at the outer midplane, showing that the electron temperature and density increase but the parallel Mach number decreases significantly due to the gas injection. Effects of poloidal $E \times B$ drifts and parallel SOL flows on the divertor asymmetry observed in EAST are also discussed. © *2014 AIP Publishing LLC*. [http://dx.doi.org/10.1063/1.4863843]

## I. INTRODUCTION

Divertor target power distribution is an important issue for the next step tokamak fusion devices. Divertor asymmetry in target heat flux has been discussed in several tokamaks, such as JT-60U,[1–3] JET,[4–6] ASDEX-Upgrade,[7,8] DIII-D,[9,10] Alcator-C Mod,[11] and NSTX.[12] Usually, the outer divertor receives large power in normal field (ion $\nabla B$ drift direction towards the lower divertor) for lower single null (LSN) configuration, while the divertor asymmetry is balanced or even inboard enhanced in reversed field (ion $\nabla B$ drift direction away from the lower divertor).[3,11,13,14] Several mechanisms have been proposed to interpret the divertor asymmetry, such as Shafranov shift, divertor geometry, divertor radiation, $\mathbf{B} \times \nabla B$ drift, diamagnetic drift, $\mathbf{E} \times \mathbf{B}$ drifts, parallel scrape-off layer (SOL) flow, and ballooning-like transport. The poloidal $\mathbf{E} \times \mathbf{B}$ drift in SOL plays an important role in divertor asymmetry, enhancing the outer divertor particle flux in normal field for LSN configuration.[15] A model based on modified Bohm boundary condition indicates that the poloidal $\mathbf{E} \times \mathbf{B}$ drift directed towards the target plate leads to a decrease in density and increase in temperature.[16] The gas puff-and-pump divertor experiment results show that the poloidal $\mathbf{E} \times \mathbf{B}$ drift across the private flux region (PFR) dominates the particle transport between the inner and outer divertors in DIII-D,[9,17] which is demonstrated by UEDGE code.[18]

Parallel SOL flow has a strong effect on divertor asymmetry due to the fast parallel transport along magnetic field.[1] The parallel SOL flow at various poloidal locations has been measured in many tokamaks, such as JT-60U,[19] JET,[20] ASDEX-Upgrade,[21,22] DIII-D,[23] Alcator C-Mod,[24] NSTX,[25] Tore Supra,[26] and TCV.[27] The absolute value and direction of parallel flow measured in low-field side (LFS) SOL are in good agreement with the Pfirsch-Schlüter (PS) flow.[28] The parallel flow consists of two components: one is the $B_T$-dependent flow which refers to classical drifts; the other one is the $B_T$-independent flow, e.g., ballooning-like flow.[29] Both the two components have significant effects on divertor asymmetry.

Divertor asymmetry during helium puffing is investigated in various divertor configurations on Experimental Advanced Superconducting Tokamak (EAST). The paper is organized as follows. Section II describes related diagnostics and experimental setup. Section III gives the experiment results about divertor asymmetry, parallel SOL flow and divertor radiation. Section IV is a discussion. Conclusions are presented in Sec. V.

## II. EXPERIMENTAL SETUP

EAST is a superconducting tokamak with a modern divertor configuration ($R_0 \sim 1.88$ m, a $\sim 0.45$ m, $B_T < 3.5$ T).[30] EAST has a flexible poloidal field control system to accommodate LSN, double null (DN), and upper single null (USN) divertor configurations. Graphite tiles were replaced with molybdenum tiles on the low heat load area of the plasma facing

a)Email: lshch@ipp.ac.cn

 © 2014 AIP Publishing LLC

This article is copyrighted as indicated in the article. Reuse of AIP content is subject to the terms at: http://scitation.aip.org/termsconditions. Downloaded to IP: 192.38.67.112 On: Thu, 25 Dec 2014 10:55:46

components (PFC) to reduce recycling and facilitate high-performance operation in 2011, but the graphite tiles remained on the divertor target plates. An in-vessel cryopump was installed under the lower outer passive target blanket to enhance the gas pump efficiency,[31] as shown in Fig. 1. EAST has achieved 410 s steady-state long pulse divertor operation in the 2012 experimental campaign after wall conditioning by lithium evaporation.

Divertor probes are configured as 74 triple probes which consist of 222 Langmuir probes embedded in the divertor target tiles to measure ion saturation current $j_{sat}$, electron temperature $T_e$, and the electron density $n_e$ at the four divertor targets (UI-upper inner, UO-upper outer, LI-lower inner, LO-lower outer) with a spatial resolution of 15 mm and 10 mm at the inner and outer divertor target plates, respectively, as shown in Fig. 1.[32] The temporal resolution of the divertor probes is 20 $\mu$s. The particle flux $\Gamma_t$ and heat flux $q_t$ at target are derived from Langmuir probes with the formulas as follows:

$$\Gamma_t = n_t c_{st} \sin\theta = n_t \sqrt{2kT_e/m_i} \sin\theta, \quad (1)$$

$$q_t = \gamma k T_t \Gamma_{\parallel} \sin\theta, \quad (2)$$

where $\theta$ is the angle between the magnetic field line and the target plate plane, and $\gamma \approx 7$ is the sheath heat transmission coefficient. The total target power deposition is given by integrating the heat flux at the four target plates

$$P = \sum_{i=1}^{4} P_i = \int_{s_a}^{s_b} 2\pi R_{div} q_t(R_{div}, s) ds, \quad (3)$$

where s is the poloidal coordinate along the target plate, $R_{div}$ is the major radius of the divertor probe, $P_i$ (i = 1, 2, 3, 4, corresponding to UI, UO, LI, LO divertor target, respectively) is the power load at each plate, and P is the total power deposition at all the four targets.

Reciprocating probes are used to measure the edge floating potential $V_f$, electron temperature $T_e$, electron density $n_e$, and the parallel Mach number in the LFS SOL,[33] with the temporal resolution of 1 $\mu$s. The divertor radiated power is measured by two absolute extreme ultraviolet (AXUV) array, with one array viewing the lower divertor from the plasma top and the other array viewing the whole plasma from the LFS midplane.[34,35] A new dual gas puff imaging (GPI) system has been installed with up-down symmetry views in EAST, measuring the edge turbulence structure and velocity, with a temporal resolution of 400 kHz and spatial resolution of 2 mm,[36] as illustrated in Fig. 1. A total of 200 Pa l helium gas is injected into the plasma edge for each GPI view for ~250 ms. It should be noted that the gas puff intensity of the upper GPI is much smaller than the lower one, mainly due to the obstruction in the upper GPI gas tube.

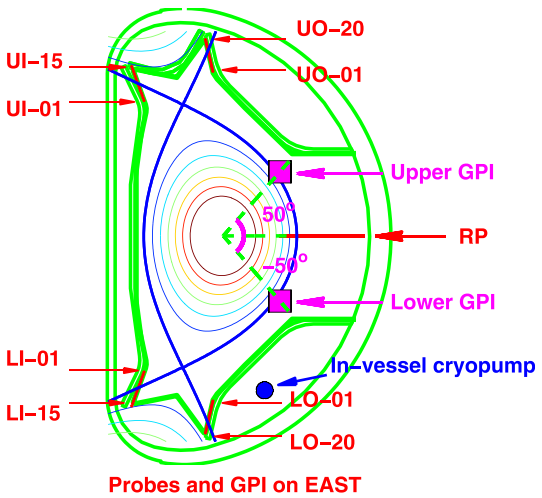


FIG. 1. Diagnostic setup in EAST, including divertor probes at four target plates, reciprocating probes at the LFS midplane, two GPI views on LFS and the in-vessel cryopump under the LO passive target blanket.

## III. EXPERIMENTAL RESULTS

A series of experiments have been carried out in EAST to study the effects of helium gas puffing on divertor asymmetry. The typical discharge conditions are illustrated in Fig. 2, with plasma current $I_p = 400$ kA, toroidal field $B_T = -2$ T in reversed field (anti-clockwise direction viewing from the plasma top, i.e., ion $\nabla B$ drift direction away from the lower divertor), line averaged electron density $\bar{n}_e = 2 \sim 2.3 \times 10^{19} m^{-3}$ before gas puff and $2.5 \sim 2.9 \times 10^{19} m^{-3}$ after gas puff, the Ohmic heating power $P_{Ohmic} = 0.33$–$0.38$ MW, and no auxiliary heating power. The $dR_{sep}$ of shot #41606, #41608, and #41610 defined as the distance between the two X points mapped to LFS midplane are 0.1, −3.2, and 3.2 cm, corresponding to DN, LSN, and USN configurations, respectively. The reciprocating probe at the LFS midplane makes two strokes to measure the edge plasma parameters at 5.2 s and 7.1 s. The control signal of GPI gas puff valve is shown in Fig. 2(g), with helium gas puff from 6 to 6.3 s. As seen from Fig. 2, the gas puff leads to an increase in plasma density $\Delta\bar{n}_e =\sim 0.5 \times 10^{19} m^{-3}$ and an increase in plasma stored energy ~10%, which indicates that the amount of gas puff does not result in a strong cooling effect. In these experiments, the effects of helium puffing on divertor asymmetry can be investigated at various divertor configurations with otherwise identical conditions.

In a steady-state discharge, divertor power plus the radiated power should be close to the total input power. The power balance is analyzed in these L-mode Ohmic discharges, as shown in Fig. 3. The total radiated power of the whole plasma $P_{rad}$ is measured by the resistive bolometer,[37] and the power loading on the divertor targets $P_{div}$ is measured by the infra-red (IR) camera.[38] The portion of radiated power in the total input power is 30%–40%, and the divertor target power is about 40%–60% of the input power. For the three shots #41606 (DN), #41608 (LSN), and #41610 (USN), the total radiated power increases ~10% due to the helium gas injection. The divertor power decreases after the gas injection in both the DN and LSN configurations, while increases in USN configuration. The sum of $P_{rad}$ and $P_{div}$ is a little smaller than the input power $P_{OH}$, indicating that a small part of the input power probably deposit on the first wall which is not monitored by the IR camera. The experimental results show a good power balance in our experiments.

This article is copyrighted as indicated in the article. Reuse of AIP content is subject to the terms at: http://scitation.aip.org/termsconditions. Downloaded to IP: 192.38.67.112 On: Thu, 25 Dec 2014 10:55:46

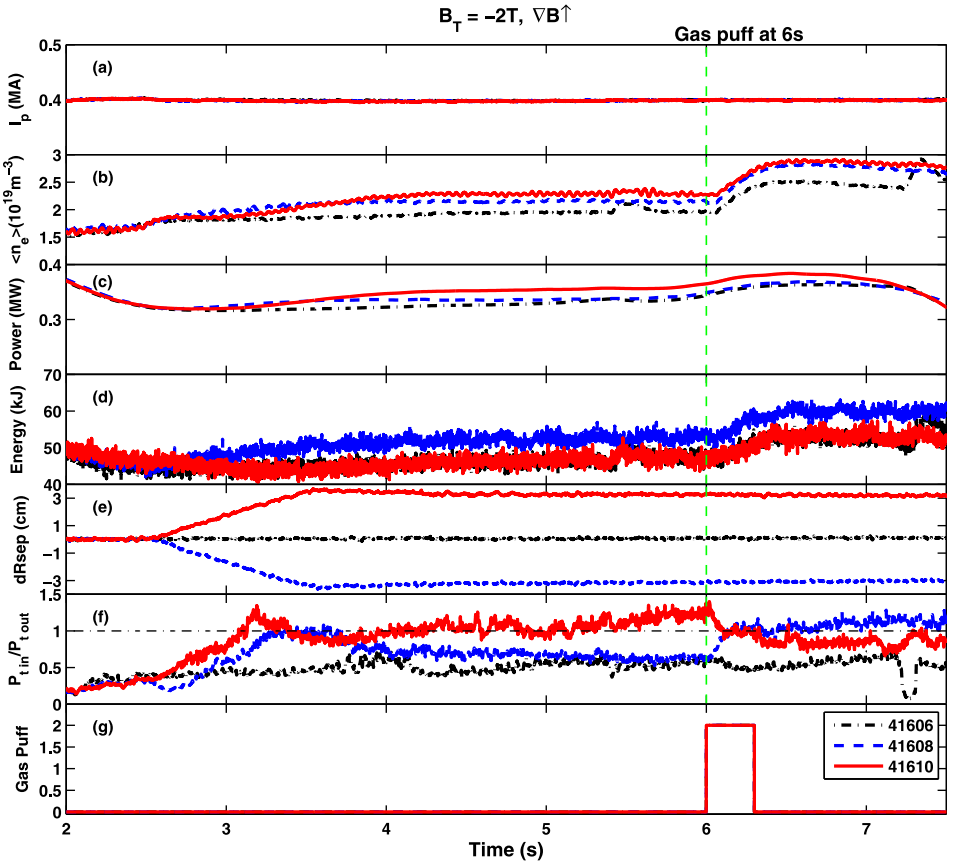


FIG. 2. The discharge conditions of shot #41606 (black pecked line), #41608 (blue dashed line), and #41610 (red solid line). (a) plasma current; (b) line averaged density; (c) the Ohmic heating power; (d) plasma stored energy; (e) $dR_{sep}$; (f) the in-out power asymmetry ratio measured by divertor Langmuir probes; (g) the valve control signal of GPI.

As predicted by the two-point model, the static pressure at the divertor target would be approximately half of the upstream pressure, i.e., $2n_{et}T_{et} = n_{eu}T_{eu}$, derived from the parallel power balance in the SOL region.[39] The upstream and target pressure showed in Fig. 4 is in perfect agreement with the two-point model, indicating that the measurements at the outer midplane and divertor target are consistent with each other.

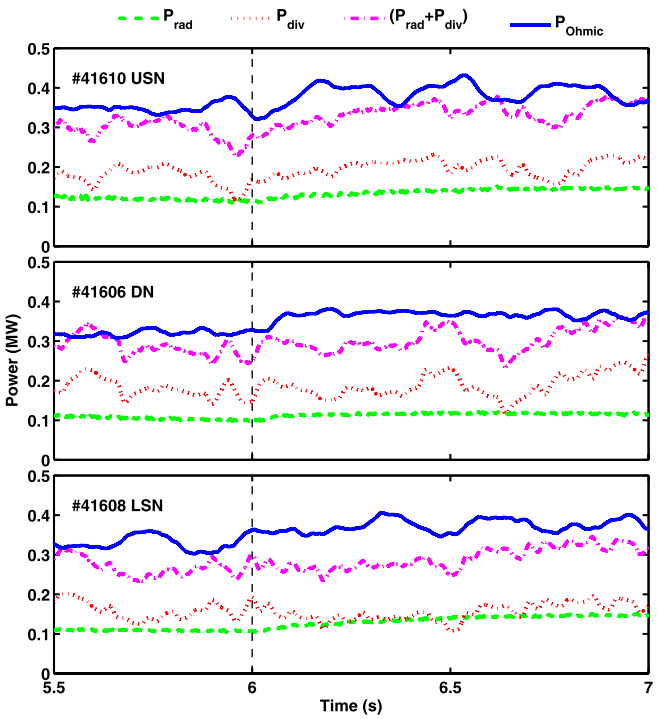


FIG. 3. The evolution of the total radiated power measured by resistive bolometer $P_{rad}$, the divertor target power measured by IR camera $P_{div}$, ($P_{rad}$ + $P_{div}$), and the Ohmic heating power $P_{Ohmic}$.

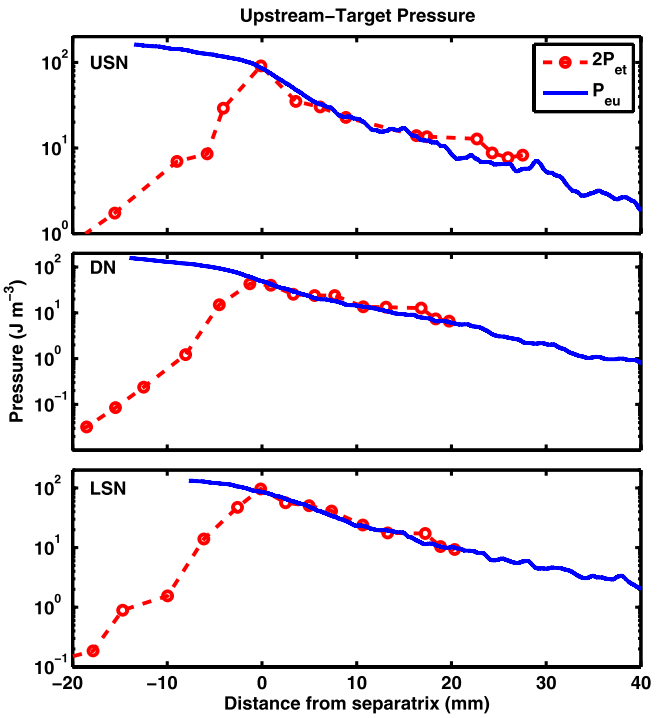


FIG. 4. The relationship between upstream and target pressures in the post-GPI phase of shot #41610 (USN), #41606 (DN), and #41608 (LSN). The red dashed line (circle) is the target electron pressure multiplied by a factor of 2, and the blue solid line is the upstream electron pressure.

This article is copyrighted as indicated in the article. Reuse of AIP content is subject to the terms at: http://scitation.aip.org/termsconditions. Downloaded to IP: 192.38.67.112 On: Thu, 25 Dec 2014 10:55:46

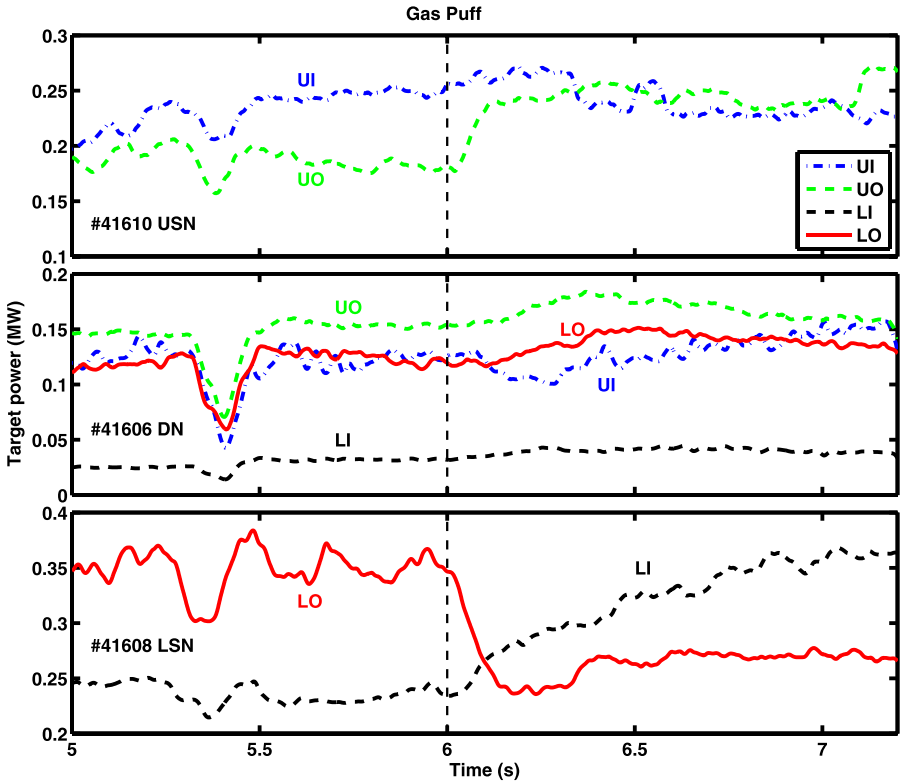


FIG. 5. The total power deposition at target plates measured by divertor Langmuir probes in USN, DN, and LSN divertor configurations.

### A. Divertor asymmetry

The power deposition at each divertor target plate and all the four targets are given by Eq. (3). The evolution of power at the four divertor targets measured by divertor Langmuir probes in USN, DN, and LSN configurations is illustrated in Fig. 5. The heat flux measured by divertor Langmuir probes is consistent with that measured by IR camera.[40] The heat flux from divertor Langmuir probes during Ohmic discharge is 2–3 times larger than that from IR camera, mostly due to that the sheath transmission factor $\gamma$ is not a constant[41] and the uncertainty of the probe and IR camera. However, the target power deposition from IR camera shows the same characteristics as that from divertor probes, as illustrated from Fig. 5.

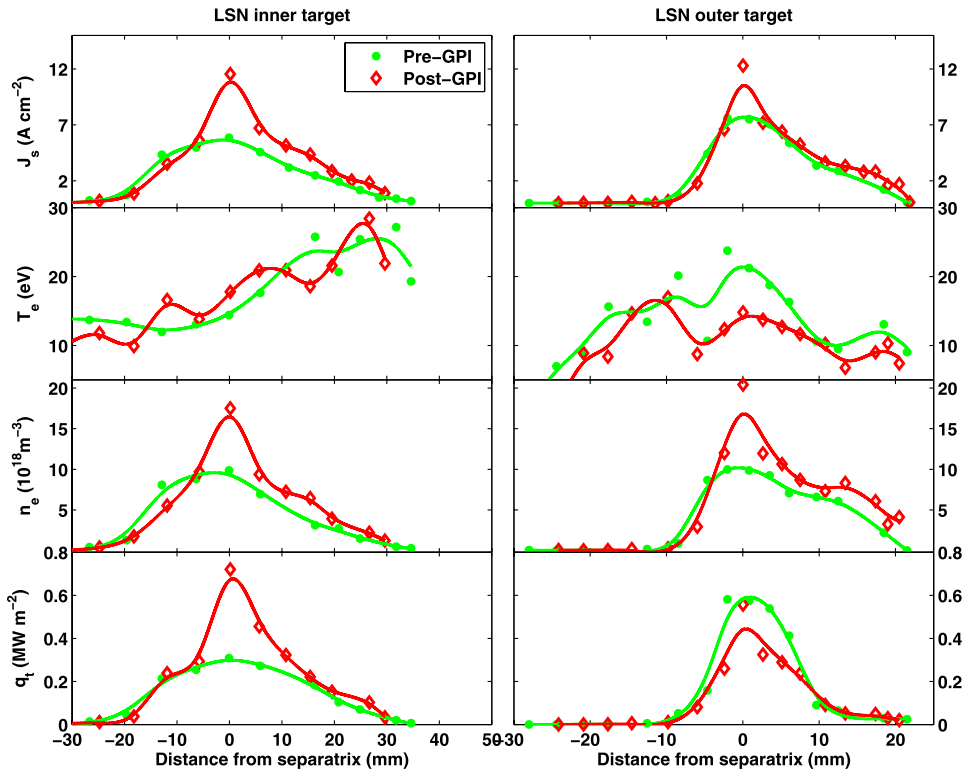


FIG. 6. Profiles of Langmuir probe at LI and LO target plates in LSN configuration (#41608). The distance from the separatrix is mapped to the LFS midplane. The parameters are the ion saturation current $j_s$, $T_e$, $n_e$, and heat flux $q_t$. The green star is the averaged data in the pre-GPI phase, corresponding to 5.6–6 s; the red diamond is the averaged data in the post-GPI phase, corresponding to 6.8–7.3 s.

This article is copyrighted as indicated in the article. Reuse of AIP content is subject to the terms at: http://scitation.aip.org/termsconditions. Downloaded to IP: 192.38.67.112 On: Thu, 25 Dec 2014 10:55:46

Since the temporal resolution of divertor Langmuir probe is much higher than that of IR camera, and divertor probe can provide more plasma parameters ($j_s$, $T_e$, $n_e$) than IR camera, it is better to select the divertor probe to analyze divertor asymmetry. It should be noted that the sudden drops of target power deposition at 5.2 s and 7.1 s are caused by the strokes of reciprocating probes. For LSN topology, the power of LO target is much larger than that of the LI target before gas puff, exhibiting a strong in-out asymmetry. After the gas puff at 6 s, the power of the LO target decreases significantly in a short time of ~0.1 s, while the power of the LI target increases gradually in a relatively long time of ~0.8 s. Obviously, the outer divertor is cooled by the gas puff. For USN topology, an inboard enhanced divertor power asymmetry appears before gas puff. After the gas puff, the power of the UO target increases rapidly during a short time of ~0.2 s, while the power of the UI target is kept at an almost constant level. For DN topology, the UO target has the largest deposition power, the UI and LO targets are the next and the LI target is the last. The power of both the UO and LO targets increases a little, while the power of the UI target decreases a little.

The divertor in-out asymmetry in target power deposition is defined as follows: $P_{t,in}/P_{t,out} = P_{LI}/P_{LO}$ for LSN, $P_{t,in}/P_{t,out} = P_{UI}/P_{UO}$ for USN, and $P_{t,in}/P_{t,out} = (P_{UI} + P_{LI})/(P_{UO} + P_{LO})$ for DN. The divertor asymmetry evolutions for various divertor topologies are shown in Fig. 2(f). The outboard enhanced divertor power asymmetry changes to a weak inboard enhanced asymmetry in LSN, while the inboard enhanced divertor power asymmetry changes to a weak outboard enhanced asymmetry in USN. For DN configuration, the outboard enhanced divertor power asymmetry increases a bit due to the gas injection. Strong effects of helium gas injection on divertor asymmetry are observed in these experiments.

Detailed divertor plasma profiles of the two phases in the LSN configuration are shown in Fig. 6, i.e., prior to the gas puff (pre-GPI) and right after the gas puff (post-GPI). The error bars of ion saturation current $j_s$ were caused mainly by the effective collecting area of the probe tips, with a systematic error of about ±10%. The scatter of the data which is probably induced from fluctuations can cause a stochastic error additionally. All the target data are averaged during 0.4–0.8 s time in order to reduce the error. The errors of electron temperature $T_e$ measured by divertor triple probes are estimated to be roughly ±50%, based on the comparison with divertor single probe measurements in previous EAST experiment.[40] According to the error transfer formula, the error of electron density $n_e$ is about ±35%. The target power $q_t$ consists of the kinetic power $q_k$ and the potential power $q_P$[39]

$$q_t = q_K + q_P = (\gamma T_t + \varepsilon_{pot}) n_t c_{St} = (\gamma T_t + \varepsilon_{pot}) j_s / e, \quad (4)$$

where $\gamma$ is sheath transmission coefficient, $\varepsilon_{pot}$ is the potential energy per incident ion, including the ionization potential of a hydrogenic ion (13.6 eV) and half of the binding energy of a hydrogenic molecule (approximately 2.2 eV), thus $\varepsilon_{pot} \sim 16$ eV. If $\varepsilon_{pot} \ll \gamma T_e$, $dq_t/q_t \approx dT_e/T_e + dj_s/j_s$, i.e., ~±60%. In the region where $\gamma T_e$ is comparable to $\varepsilon_{pot}$, the error of $q_t$ is determined mainly by the error of $j_s$ measurement, i.e., ~±10%. As shown in Fig. 6, the shapes of $q_t$ profiles are the same as $j_s$, demonstrating the error of $q_t$ is determined by $j_s$. Since all the data here measured by divertor Langmuir probes are time-averaged value, the relationship of electron pressure between divertor target and upstream is consistent with the two-point model, demonstrating that the errors of parameters measured by divertor probes are acceptable. In the pre-GPI phase, the LO target has larger $j_s$, $T_e$ and peak heat flux $q_t$ near the strike point than the LI target, with balanced density $n_e$ for the two targets. In the post-GPI phase, though the $j_s$ and $n_e$ at the LO target increase

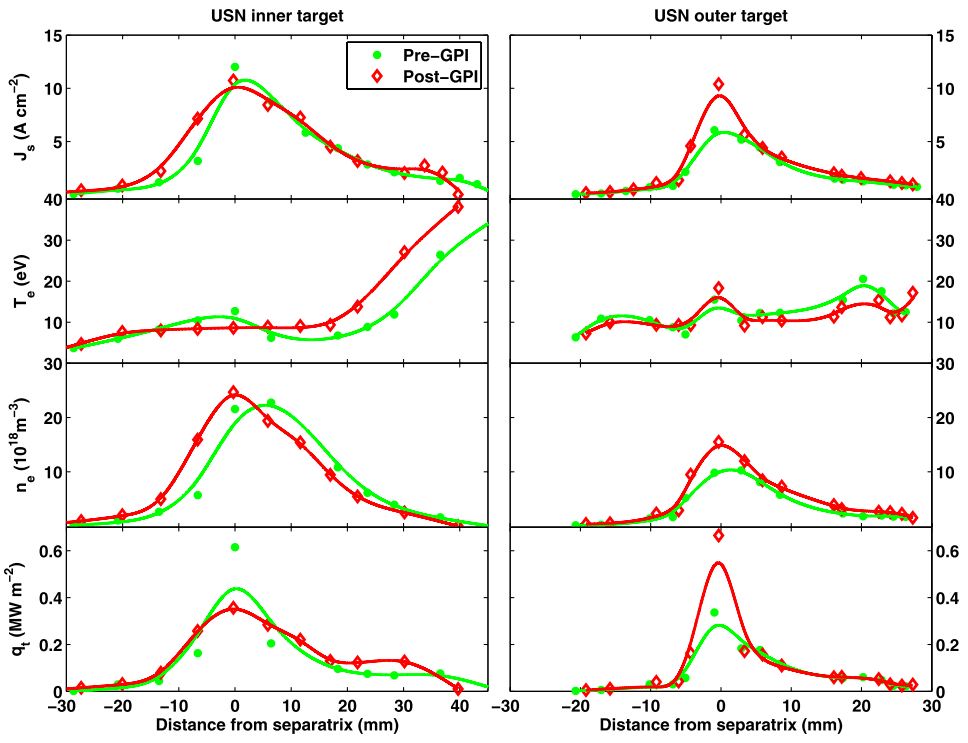


FIG. 7. Profiles of Langmuir probe at UI and UO target plates in USN configuration (#41610). The green star is the averaged data in the pre-GPI phase, corresponding to 5.6–6 s; the red diamond is the averaged data in the post-GPI phase, corresponding to 6.2–7 s.

This article is copyrighted as indicated in the article. Reuse of AIP content is subject to the terms at: http://scitation.aip.org/termsconditions. Downloaded to IP: 192.38.67.112 On: Thu, 25 Dec 2014 10:55:46

evidently, the $T_e$ reduces significantly leading to a much lower heat flux $q_t$ compared to the pre-GPI phase. In contrast to the LO target, the parameters of the LI target increase significantly, especially the peak value of $j_s$, $n_e$, and $q_t$. It is clear that the sharp drops of the heat flux at the LO target are due to the large decrease of $T_e$.

Divertor profiles in the USN configuration are shown in Fig. 7. In the pre-GPI phase, the UI target has a larger peak $j_s$, $n_e$, and $q_t$ than the UO target. In the post-GPI phase, the $T_e$ of UO target decreases a little, but the $n_e$ increases dramatically, which leads to a large increase of peak heat flux. The effect of gas injection on the UI target is very weak, which is consistent with the total power deposition at the UI target. It should be noted that the cooling effect at the UO target in USN due to the gas puff is much weaker than the LO target in LSN, therefore the divertor asymmetry in target power deposition favors the outer target in USN configuration in the post-GPI phase, as illustrated in Fig. 2(f).

Divertor profiles in the DN configuration are shown in Figs. 8 and 9. In the pre-GPI phase, the peak heat fluxes at the UI and UO targets are almost equal and larger than that of the LO target, and the peak heat flux of LI target is the lowest one. In the post-GPI phase, the peak heat flux of LI target is the smallest one, and the other three targets have equal peak heat fluxes. The helium gas injection leads to an evident decrease of $T_e$ at the UO and LO plates, and a large increase of $n_e$ at all the divertor plates except for the LI target. The gas puff effect on divertor heat flux is relatively weak in DN compared to single null (SN) configuration. It should be noted that the peak heat flux at the target in DN is smaller than that of SN configuration.

## B. Parallel SOL flow

The edge plasma parameters and parallel SOL flow velocity in the outer midplane SOL are measured by reciprocating probes in both the pre-GPI (5.2 s) and the post-GPI (7.1 s) phases, as illustrated in Fig. 10. In contrast to the pre-GPI phase, the $n_e$ and $T_e$ of LSN topology in the post-GPI phase increase significantly, leading to a relatively high electron pressure presumably due to the increase of Ohmic heating power and plasma stored energy. The $n_e$ increases evidently while the $T_e$ increases slightly in DN and USN configurations. The parallel Mach number is shown at the bottom of Fig. 10, with the maximum value of $|M_{||}|$ near the separatrix in the range of 0.3–0.5, corresponding to the velocity of $|V_{||}| = 30 - 50\,\mathrm{km/s}$. It should be noted that the maximum of $|M_{||}|$ in LSN is much smaller than the DN and USN configurations, i.e., the plasma rotation is smaller in LSN topology. The measured parallel SOL flow in EAST is consistent with the PS flow.[42] Since these discharges are in reversed field, the PS flow is from the plasma top to the bottom that is in the same direction as the measured parallel flow. The parallel Mach number decreases significantly in the post-GPI phase, presumably due to the enhancement of density caused by the gas injection, which is a key characteristic of the PS flow.

Components of the poloidal particle flux produced by the parallel SOL flow and the poloidal $\mathbf{E}\times\mathbf{B}$ drift are analyzed, as illustrated in Fig. 11. The total poloidal particle flux in SOL is calculated by integrating the parallel flow component ($V_{||}\Theta$) and the poloidal $\mathbf{E}\times\mathbf{B}$ drift component ($V_{\mathbf{E}\times\mathbf{B}}\phi$) across the SOL from separatrix (0) to the outermost radius ($\lambda_{SOL}$)[43]

$$\Gamma_\theta = \int_0^{\lambda_{SOL}} 2\pi R\left(n_i V_{||}\Theta + n_i V_{E\times B}\phi\right)dr, \tag{5}$$

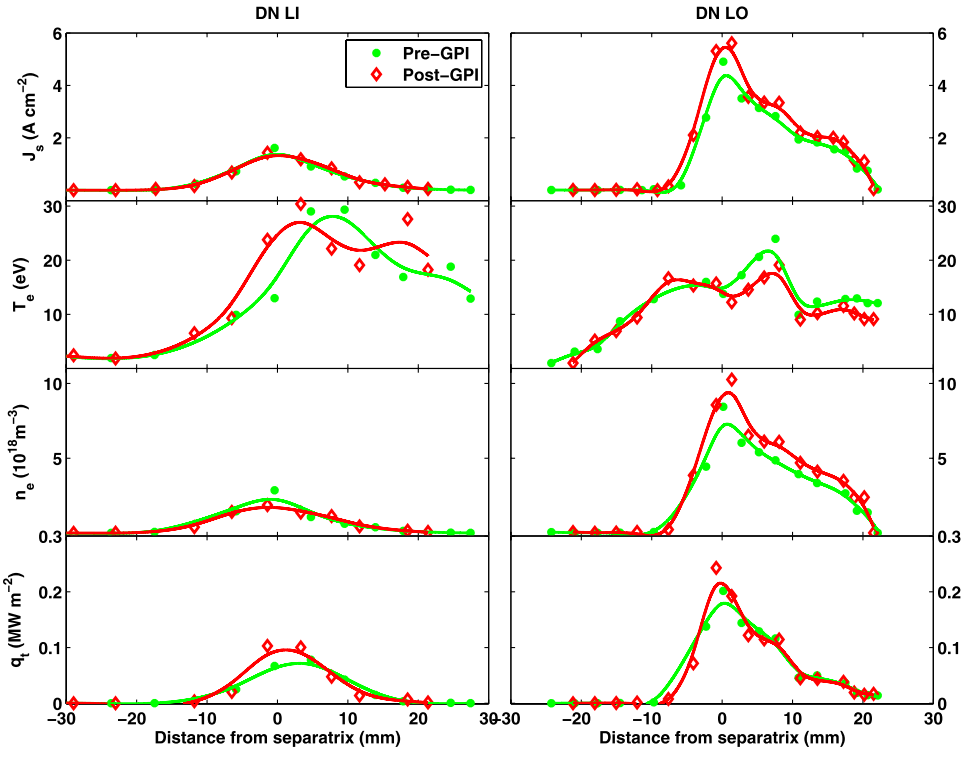


FIG. 8. Profiles of Langmuir probe at LI and LO target plates in DN configuration (#41606). The green star is the averaged data in the pre-GPI phase, corresponding to 5.6–6 s; the red diamond is the averaged data in the post-GPI phase, corresponding to 6.6–7 s.

This article is copyrighted as indicated in the article. Reuse of AIP content is subject to the terms at: http://scitation.aip.org/termsconditions. Downloaded to IP: 192.38.67.112 On: Thu, 25 Dec 2014 10:55:46

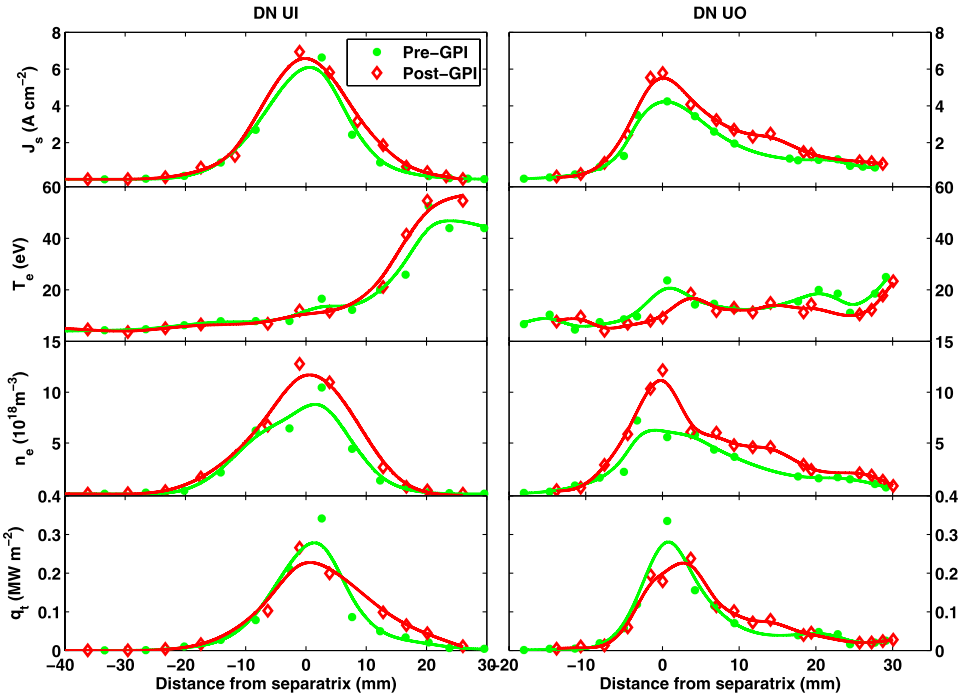


FIG. 9. Profiles of Langmuir probe at UI and UO target plates in DN configuration (#41606). The green star is the averaged data in the pre-GPI phase, corresponding to 5.6–6 s; the red diamond is the averaged data in the post-GPI phase, corresponding to 6.6–7 s.

where $\Theta = B_\theta/B_\parallel \approx B_\theta/B_0$, $\phi = B_T/B_\parallel \approx 1$. The radial electric field $E_r$ is estimated by the calculated mean phase velocity of turbulence, ignoring the turbulence phase velocity in the plasma frame.[44–47] In reversed field, the parallel flow component is directed downwards, and the poloidal $\mathbf{E}\times\mathbf{B}$ drift component directed upwards in the main SOL. The total poloidal particle flux directed downwards increases steeply near the separatrix at outer midplane, dominated by the parallel flow component. It is obvious that the total poloidal particle flux in LSN configuration is smaller compared to the other two configurations. The total poloidal particle flux at outer midplane is calculated by integrating $\Gamma_\theta$ radially from separatrix to far SOL region, as shown in Fig. 12(a). In DN and USN configurations, the total particle fluxes in post-GPI phase are ~2 times larger than that in pre-GPI phase, indicating enhanced poloidal particle flux directed

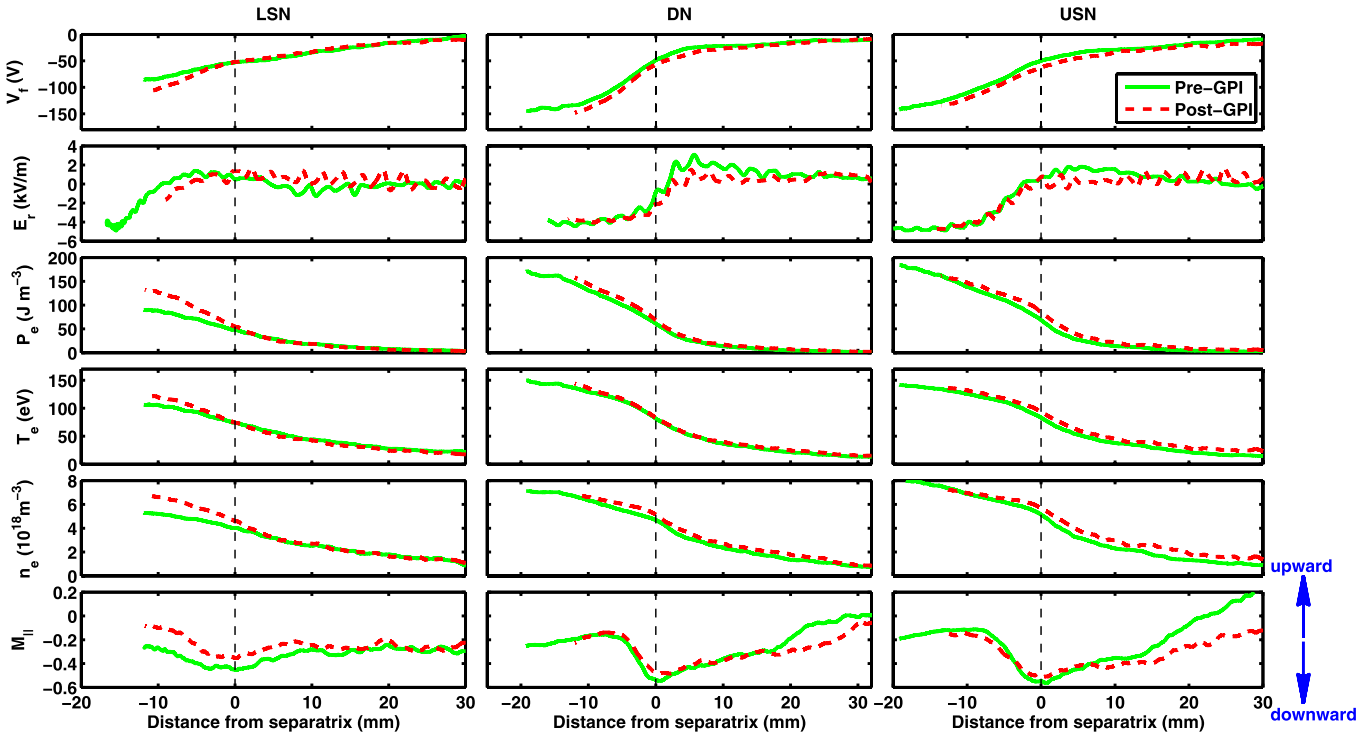


FIG. 10. The edge plasma parameters at the LFS midplane in LSN, DN and USN configurations, including the floating potential $V_f$, radial electric field $E_r$, electron pressure $p_e$, temperature $T_e$, density $n_e$, and the parallel Mach number $M_\parallel$. The positive $M_\parallel$ means that the direction of parallel flow in the poloidal plane is directed upwards at the LFS midplane, while the negative value means downwards.

This article is copyrighted as indicated in the article. Reuse of AIP content is subject to the terms at: http://scitation.aip.org/termsconditions. Downloaded to IP: 192.38.67.112 On: Thu, 25 Dec 2014 10:55:46

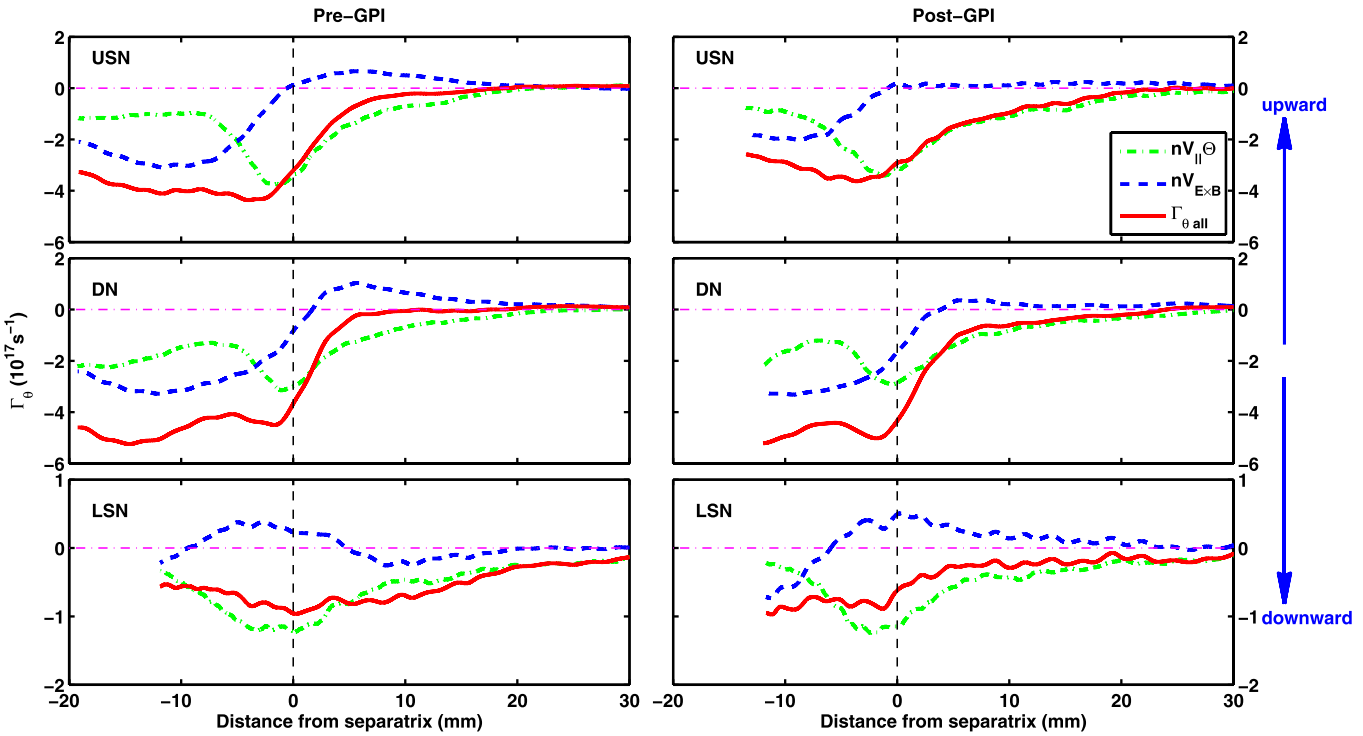


FIG. 11. Components of the poloidal particle flux produced by parallel flow ($nV_{\|}\Theta$) and poloidal $\mathbf{E}\times\mathbf{B}$ drift flow ($nV_{E\times B}$) at the outer midplane in both the pre-GPI (left panel) and post-GPI (right-panel) phases.

downwards after gas puff. Although the parallel flow component with downwards direction in post-GPI phase are a bit smaller than that in pre-GPI phase, the significant drops of the poloidal $E\times B$ drift component with upward direction make the downward total particle fluxes increase, exhibiting broad profiles in SOL region, as shown in Fig. 11. However, in LSN configuration, the poloidal $E\times B$ drift component is enhanced in main SOL in post-GPI phase compared to pre-GPI phase, which leads to smaller integrated total poloidal particle flux in post-GPI phase. In contrast to DN and USN, the integrated total poloidal particle flux is much smaller in post-GPI phases in LSN configuration. The PS flow increases with radial electrical field but deceases with $\bar{n}_e$, defined as follows:[48]

$$V_{ps} = 2q\cos\theta\left(E_r - \frac{\nabla_r p_i}{en}\right)\times\frac{B_0}{B^2}, \tag{6}$$

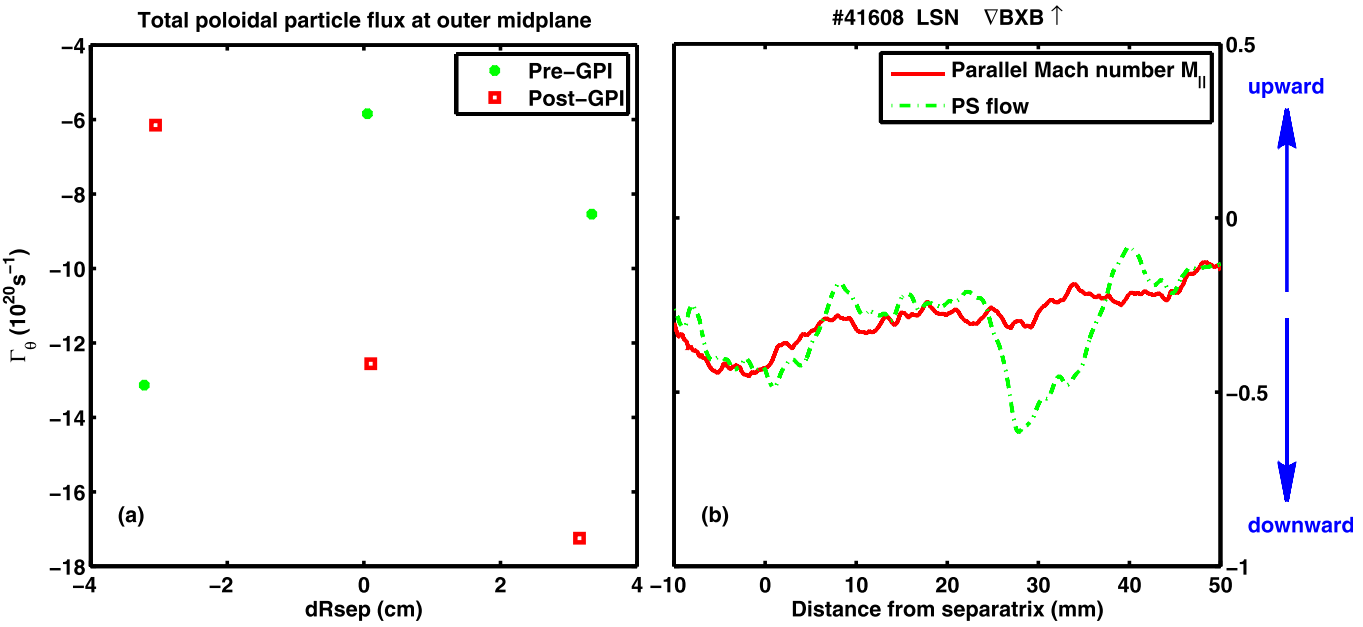


FIG. 12. (a) The total poloidal particle flux calculated by integrating radially from separatrix to far SOL region at outer midplane, directed downwards. (b) A typical parallel Mach number measured by reciprocating probes at outer midplane and the PS flow calculated from Eq. (6).

This article is copyrighted as indicated in the article. Reuse of AIP content is subject to the terms at: http://scitation.aip.org/termsconditions. Downloaded to IP: 192.38.67.112 On: Thu, 25 Dec 2014 10:55:46

where $q = rB_0/R_0B_\theta$ is the safety factor, $\theta$ is the poloidal angle with $\theta = 0$ at the outer midplane, assuming $p_e = p_i$. The PS flow is maximum and directed downwards in the outer midplane SOL in reversed field. A typical comparison between the parallel SOL flow and the PS flow is illustrated in Fig. 12(b), and they are consistent with each other well in the main SOL region.

As illustrated in Fig. 13, the radial particle flux driven by turbulence is also calculated from reciprocating probes

$$\Gamma_e = \langle \tilde{n}_e \tilde{V}_r \rangle \approx \langle \tilde{I}_s \tilde{E}_\theta \rangle n_e/(I_s B_t), \quad (7)$$

where angular brackets denote an ensemble average and $E_\theta$ is derived from the difference of floating potential at two poloidal locations. The radial particle flux is outwards in all the three divertor configurations, and enhanced by gas puff. It is smaller in LSN compared to the other two configurations. Therefore, the LSN topology has the smallest poloidal particle flux near the separatrix and turbulence-induced radial particle flux, while both of these two particle fluxes in DN topology are the largest. Turbulence-induced radial particle transport is probably closely related to the parallel flow and poloidal particle transport.

### C. Divertor radiation

Divertor radiation is measured by two XUV arrays: one array measures the radiated power in the lower divertor viewing from the plasma top; the other array measured the whole plasma, from the upper X-point to the lower X-point, as illustrated in reference.[34] The radiation distributions in both the pre-GPI phase (5.5 s) and the post-GPI phase (7 s) are shown in Fig. 14. In the pre-GPI phase, the radiated power in the LO divertor is much higher than the LI divertor in all the three divertor configurations, as shown in the left panels. From the up-down XUV array in the right panels, the main radiated power is located at the upper divertor for USN and at the lower divertor for LSN, and the DN configuration exhibits an upper divertor favored radiated power asymmetry. In the post-GPI phase, radiated power in the LO divertor in LSN configuration increases significantly compared to the pre-GPI phase, but the radiated power in the LI divertor remains unchanged. For the DN configuration, the radiation intensity in the LI divertor decreases in the post-GPI phase, while the radiation in the LO divertor remains unchanged. For the USN configuration, the radiated power in the lower divertor decreases evidently in the post-GPI phase. However, the up-down XUV array indicates that a great increase of radiated power is observed in all the three configurations in the post-GPI phase. Since the radiation measured by the XUV array is the chord-integrated intensity, not only the divertor but also the plasma along the chord makes a contribution to the measured radiation, which leads to the differences between the two XUV arrays. For the up-down XUV array, a considerable contribution to radiation may come from the LFS edge plasma, especially in the LFS gas injection experiment.

## IV. DISCUSSION

Several mechanisms are probably related to the divertor asymmetry observed in these experiments, such as the poloidal $\mathbf{E} \times \mathbf{B}$ drift and the PS flow, as illustrated in Fig. 15. Poloidal $\mathbf{E} \times \mathbf{B}$ drift in SOL is an important mechanism to influence the divertor asymmetry.[15,49] A model base on the poloidal $\mathbf{E} \times \mathbf{B}$ drift in the SOL is reported to interpret the divertor asymmetry recently.[16] Since the poloidal plasma flow associated with the poloidal $\mathbf{E} \times \mathbf{B}$ drift $V_x^{E\times B}$ is of the same order as the total particle flow to the plate $c_s b_x$ with the poloidal sound speed velocity, at the plates the following boundary condition is satisfied:

$$V_x^{E\times B} + b_x V_\parallel = c_s b_x, \quad (8)$$

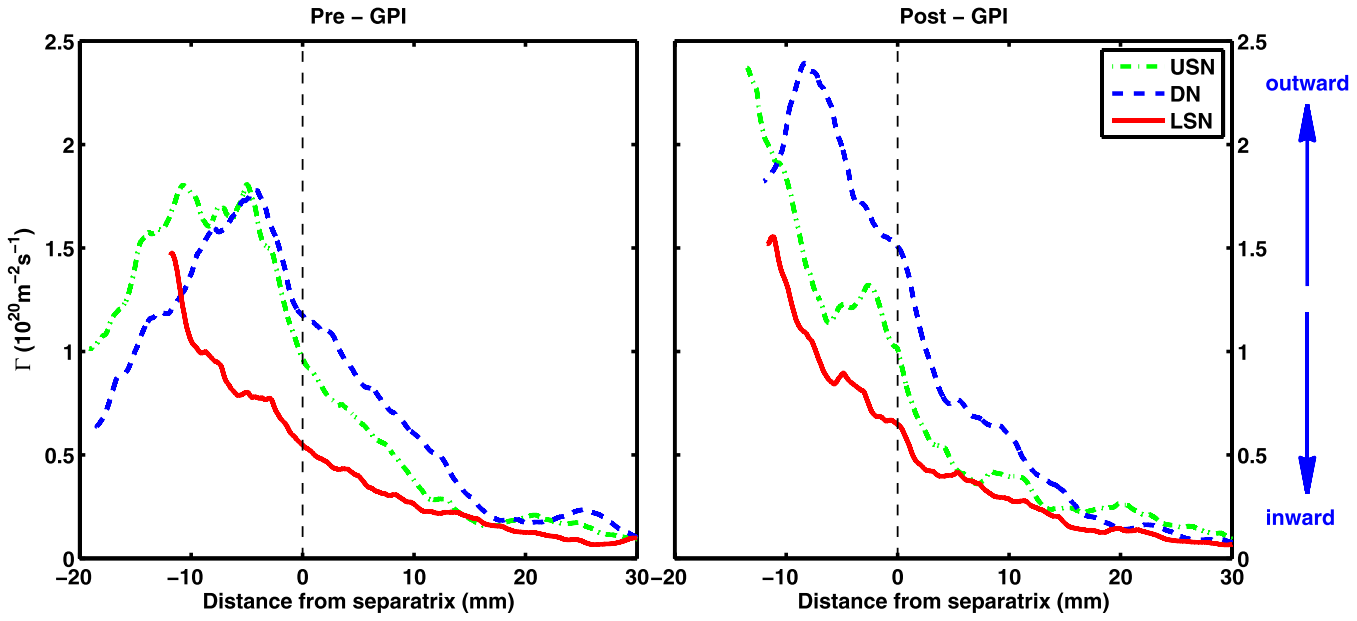


FIG. 13. The radial particle flux driven by turbulence in both Pre-GPI (left panel) and Post-GPI (right-panel) phases for LSN, DN, and USN divertor configurations.

This article is copyrighted as indicated in the article. Reuse of AIP content is subject to the terms at: http://scitation.aip.org/termsconditions. Downloaded to IP: 192.38.67.112 On: Thu, 25 Dec 2014 10:55:46

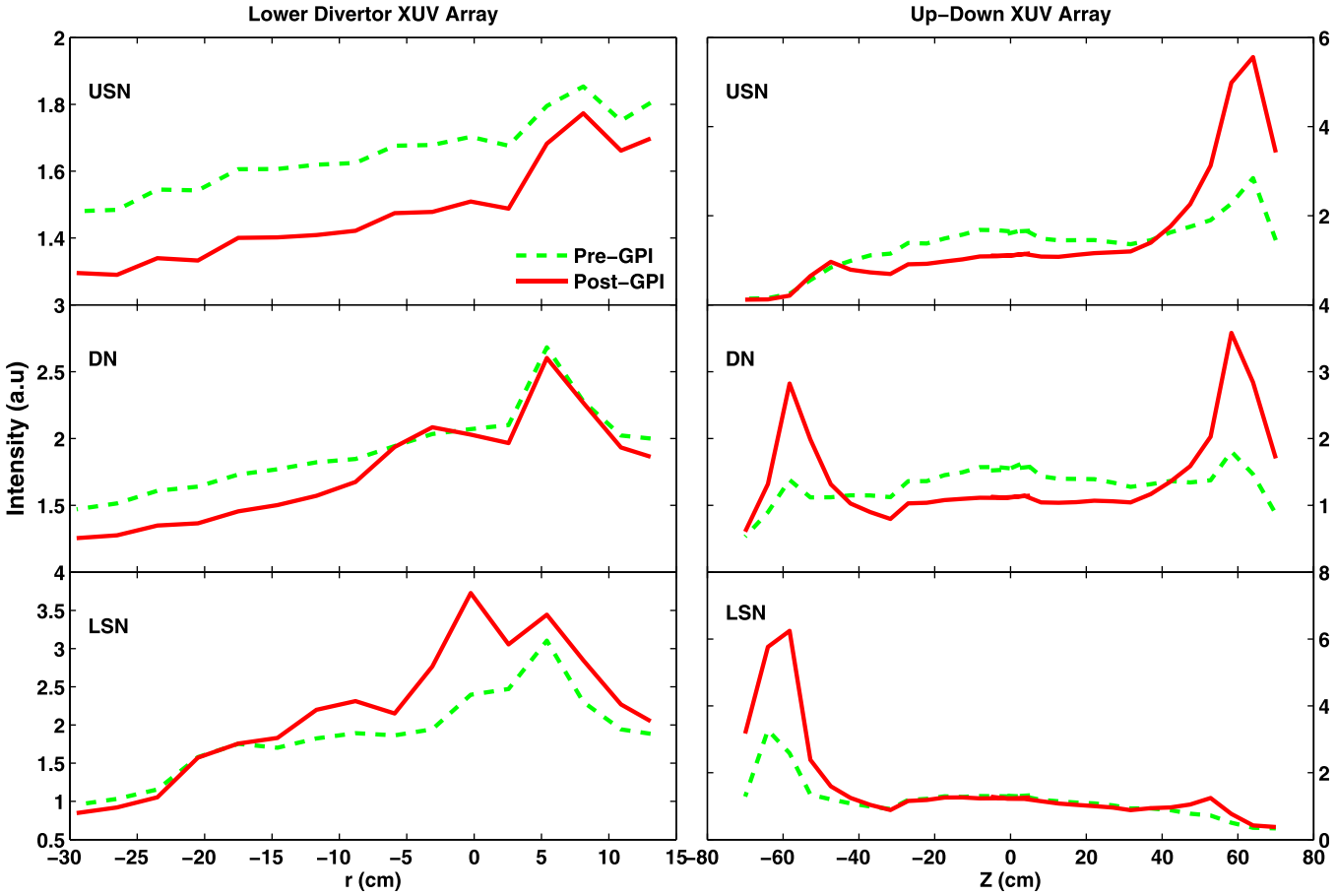


FIG. 14. The radiation profiles in both the pre-GPI phase (5.5 s) and the post-GPI phase (7 s). The data panels on the left show the radiation distribution in lower divertor, viewing from plasma top, and the horizontal axis is r = R-185 cm with R as the intersection of sight line and the horizontal line of Z = 0. Data panels on the right show the radiation distribution of the whole plasma, from the upper X-point to the lower X-point, and the horizontal axis is the Z coordinate of the intersection of sight line and the vertical line of R = 1.85 m. The sight line arrangements are shown in reference.[34]

where $b_x$ is the unit vector in the poloidal direction. In the present of drifts, the parallel velocity should adjust itself to satisfy this modified Bohm boundary condition. Consequently, for drifts directed away from the plate, the parallel flow increases, making the divertor denser and colder, while for the drifts towards the plate, the parallel flow decreases, hence decreasing the divertor density and increasing the divertor temperature. As predicted by the simulations, these effects are important in low density cases, but become very weak in high density cases.[16] Since the line averaged density is rather low, around $2 \times 10^{19} m^{-3}$ ($\sim 0.5 n_e^{GW}$) for the experiments presented here, the divertor plasma is in the low recycling, sheath-limited regime, as indicated by the parallel pressure balance along the field lines in the SOL (Fig. 4), hence, the modified Bohm boundary condition may significantly influence the divertor asymmetry. However, the poloidal $\mathbf{E} \times \mathbf{B}$ drift in SOL is considered to enhance the divertor particle flux in the same direction as drift,[15] which is in contradiction with modified Bohm boundary condition. Both these two effects of poloidal $\mathbf{E} \times \mathbf{B}$ drift are presented here to interpret our experiment results. The poloidal $\mathbf{E} \times \mathbf{B}$ drift across the PFR may also play an important role, as demonstrated by the DIII-D experiments.[9,17] The UEDGE modeling results suggest that a larger radial electrical field exists in moving into the PRF because of the rapid drop in the electron temperature there, so that the $\mathbf{E} \times \mathbf{B}$ drift across the PFR gives important contribution to particle transport.[18] As aforementioned, the parallel flow at outer midplane measured by reciprocating probes also contributes to the particle transport in SOL.

Fig. 16 shows the turbulence of upper and lower GPI diagnostics for a typical DN configuration (#41606) in Figs. 16(a) and 16(d), along with turbulence poloidal velocity $V_\theta$ in Figs. 16(b) and 16(e), and the turbulence radial velocity $V_r$ in Figs. 16(c) and 16(f), during 6 to 6.25 s. The velocity is calculated using time-delay cross-correlation method,[50] with 500 frames to obtain the velocity profile in the poloidal-radial plane vs. time. For both the upper and lower GPI, the poloidal velocity $V_\theta$ is directed upwards in LFS SOL, and the radial velocity $V_r$ is outward and enhanced in the SOL. Noted that the $V_\theta$ is in the same direction as $V_{E \times B}$, as shown in Fig. 15(b). Assuming the turbulence motion measured by GPI diagnostic is dominated by the local $\mathbf{E} \times \mathbf{B}$ flow,[51] the poloidal $V_{E \times B}$ velocity can be estimated by the $V_\theta$ measured by GPI diagnostics. The radial profiles of $V_\theta$ are illustrated in Fig. 17. The peak poloidal $V_\theta$ of upper GPI is located near the separatrix in the SOL, ~1.5 km/s for USN and DN, ~0.5 km/s for LSN; while the peak $V_\theta$ of lower GPI is ~1.6 km/s for DN, and

This article is copyrighted as indicated in the article. Reuse of AIP content is subject to the terms at: http://scitation.aip.org/termsconditions. Downloaded to IP: 192.38.67.112 On: Thu, 25 Dec 2014 10:55:46

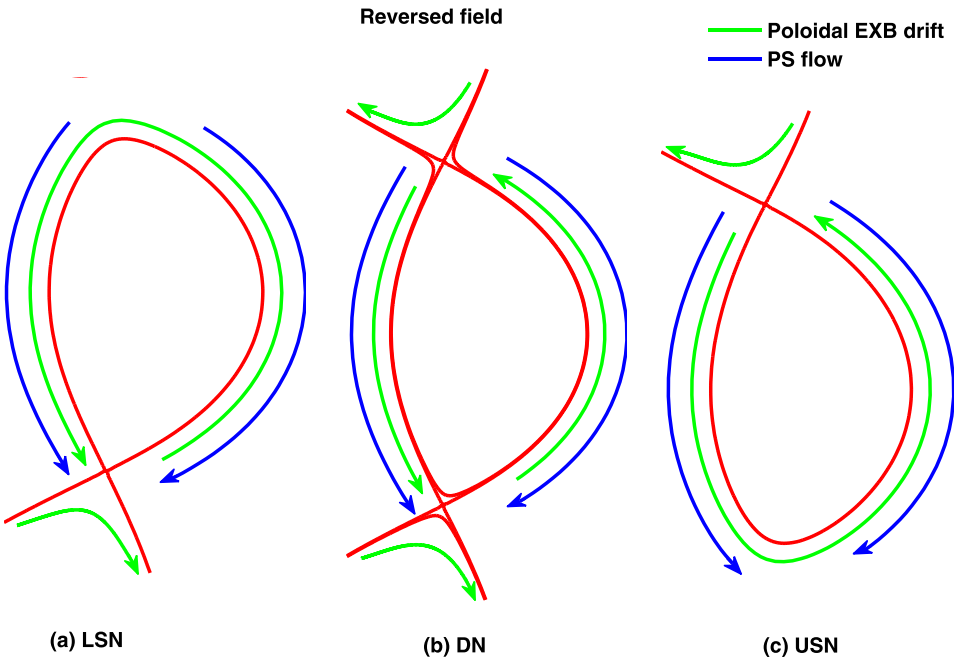


FIG. 15. Directions of the poloidal $\mathbf{E}\times\mathbf{B}$ drift and the PS flow in LSN, DN, and USN divertor configurations in reversed field.

1.2 km/s for USN and LSN. Compared to the high input power discharges in EAST,[36] the $V_\theta$ in our experiment is relatively small, indicating small poloidal $\mathbf{E}\times\mathbf{B}$ flow in SOL.

### A. LSN configuration

In the pre-GPI phase, the outer target has larger $T_e$, balanced $n_e$, and larger peak $q_t$ than the inner target in LSN configuration, as expected, because of larger outboard SOL area.

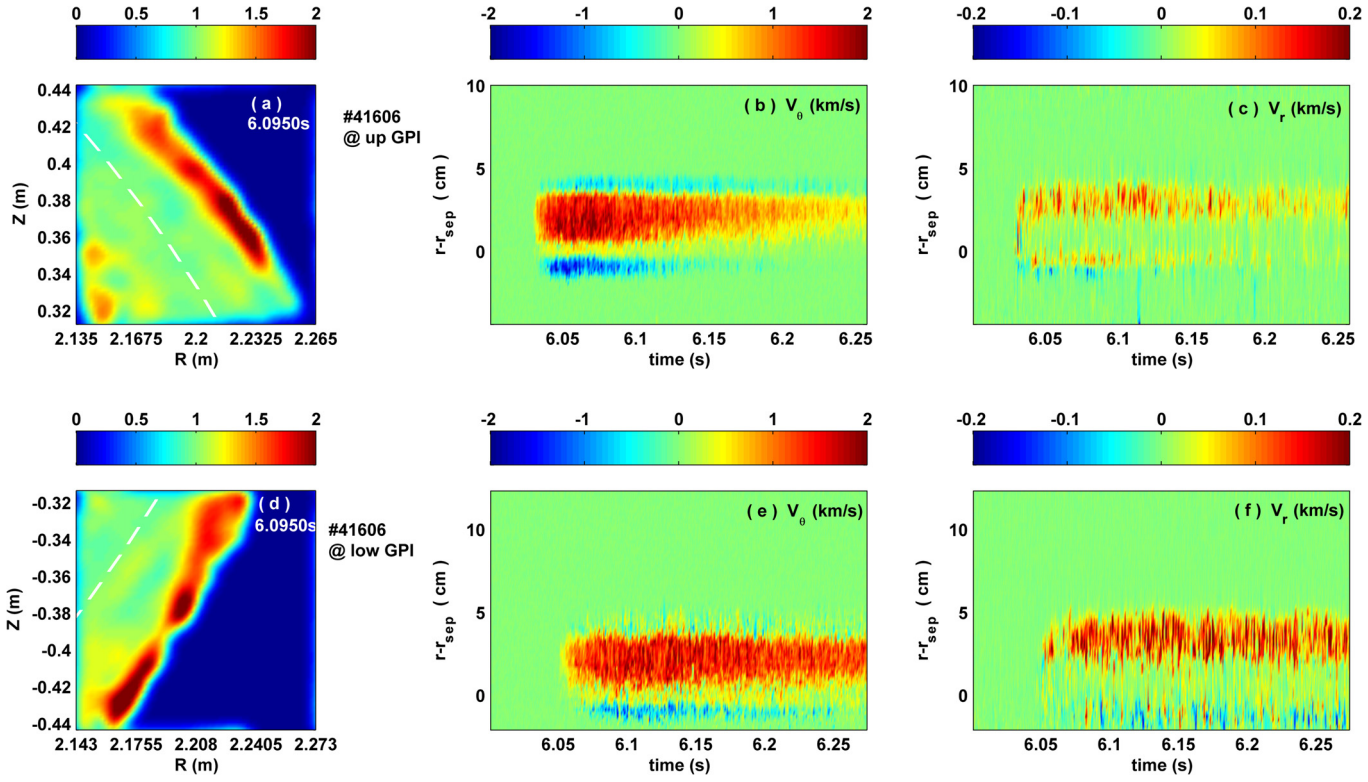


FIG. 16. Image data and velocity analysis of the upper and lower GPI diagnostic systems in an Ohmic DN configuration discharge in EAST. (a) Turbulence of upper GPI diagnostic, normalized by the time averaged emission intensity. Horizontal axis is along major radius, and the vertical axis is along vertical direction. The white dashed line is the separatrix. (b) Poloidal velocity $V_\theta$ of upper GPI diagnostic, vertical axis is the distance from separatrix along the minor radius, i.e., r-$r_{sep}$. Positive $V_\theta$ means the velocity towards the direction of ion diamagnetic drift, i.e., upwards at the outer midplane in reversed field. (c) Radial velocity $V_r$ of upper GPI diagnostic. Positive $V_r$ means the velocity outwards along the minor radius. (d) Turbulence of lower GPI diagnostic. (e) and (f) are the poloidal velocity and radial velocity of lower GPI diagnostic, respectively, with the velocity direction is the same as (b) and (c).

This article is copyrighted as indicated in the article. Reuse of AIP content is subject to the terms at: http://scitation.aip.org/termsconditions. Downloaded to IP: 192.38.67.112 On: Thu, 25 Dec 2014 10:55:46

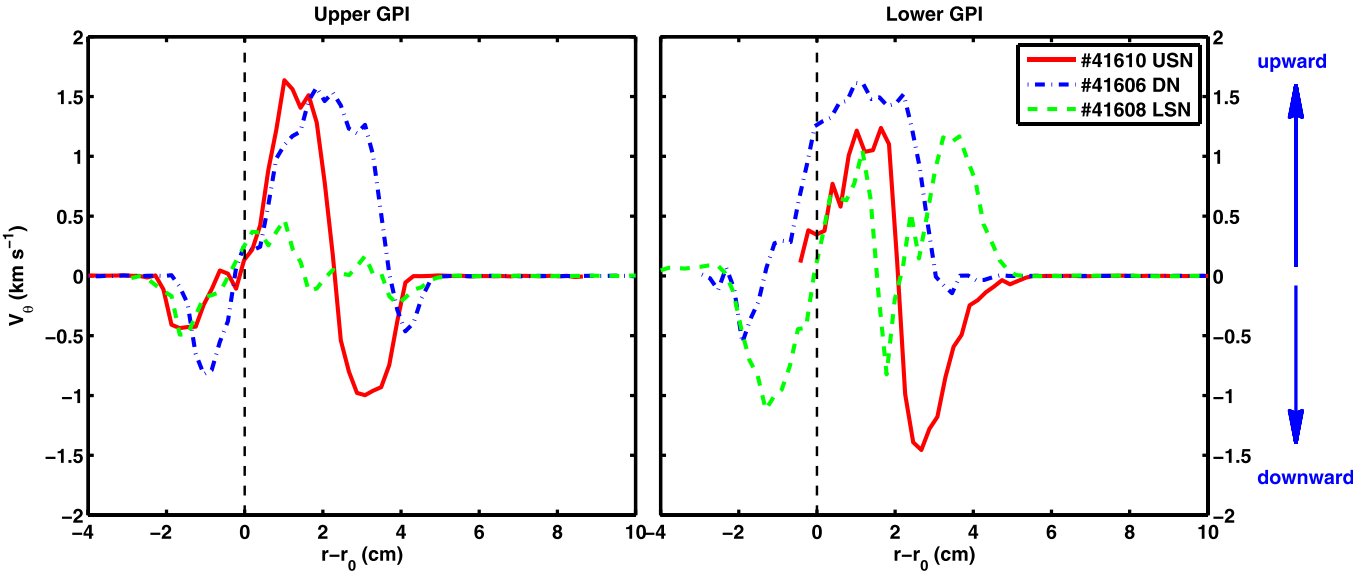


FIG. 17. The poloidal velocity $V_\theta$ measured by upper (the left panel) and lower (the right panel) GPI diagnostics, with the data averaged during the time from 6.094 to 6.097 s. The horizontal axis is the distance from separatrix along the minor radius.

As predicted by the modified Bohm boundary condition, the poloidal $\mathbf{E}\times\mathbf{B}$ drift in SOL directed away from the outer divertor target increases the parallel flow towards target, leading to larger peak $j_s$, particle and heat fluxes, as illustrated in Fig. 6. Noted that the $T_e$ near the separatrix at outer target is much larger than that at inner target, which does not agree with this model. The poloidal particle flux shown in Fig. 11 indicates the parallel flow is very important in the poloidal particle transports in SOL, favoring the outer divertor. In addition, the poloidal $\mathbf{E}\times\mathbf{B}$ drift across PRF region increases the outer divertor particle flux. Since the observations of divertor asymmetry are influenced by a large number of effects, the mechanisms listed here are considered as primary candidates contributing to the experimental results. During the post-GPI phase, the $T_e$ of LO target decreases significantly, which leads to a sharp decrease in peak heat flux. In contrast, the $T_e$ increases rapidly at LI target, while the $n_e$ increases gradually, leading to the slow increase of peak heat flux. As illustrated in Fig. 2, the line averaged density, Ohmic heating power, and plasma stored energy increase significantly due to the helium gas puffing, which may also increase the LI target heat flux.

The helium injected into plasma on LFS may change the local plasma parameters through different physical mechanisms: cooling of electrons due to dissociation and ionization of the injected helium molecules and impurity radiation, production of electrons owing to ionization of injected impurity, forces on electrons and background ions arising from collisions with impurity particles.[52] Therefore, a large portion of the injected helium molecules change to ions due to ionization, then the helium ions move along the magnetic field line and reach the divertor region. Parallel transport of impurity ions is determined by friction and thermal forces.[53] Because of the parallel flow at the outer midplane directed to the LO divertor and the short connection length between the gas injection locations and the LO divertor plate, much more helium transported to the LO divertor compared to the LI divertor can be anticipated. The total poloidal particle flux is directed to the LO divertor at outer midplane measured by reciprocating probes, as shown in Fig. 11. Furthermore, the modified Bohm boundary condition enhances the helium content at LO divertor. In addition, the in-vessel cryopump near the LO divertor enhances the SOL flow directed to the LO target, which may drag helium into the LO divertor due to the frictional force exerted by the background plasma. A high impurity content can result in large radiation at the LO target,[39] which is demonstrated by both the lower divertor XUV array and the up-down XUV array, as illustrated in Fig. 14. The LO divertor plasma is significantly cooled by helium injection.

Ions in LO divertor and LFS SOL can be transported to LI divertor by the poloidal $\mathbf{E}\times\mathbf{B}$ drift in SOL and the particle and heat fluxes at LI divertor increase slowly, though its effect may be smaller than that in DN and USN configurations, as illustrated in Fig. 11. As aforementioned, the poloidal $\mathbf{E}\times\mathbf{B}$ drift across the PFR may influence the evolution of divertor heat flux, decreasing the particle flux in the LI divertor and increasing that at the LO divertor. The radiated power measured by the lower divertor XUV array in the LI divertor remains unchanged, indicating that the impurity content is still at a low level.

### B. USN configuration

In the pre-GPI phase, the UI divertor has larger peak $n_e$ and $q_t$ than the UO divertor, in spite of larger outboard SOL area. Since the poloidal $\mathbf{E}\times\mathbf{B}$ drift in SOL is from inner divertor to outer divertor, the modified Bohm boundary condition makes the inner target denser and colder, and the consequent larger particle and heat fluxes, which is consistent with the experimental results, as shown in Fig. 7. Moreover, the poloidal $\mathbf{E}\times\mathbf{B}$ drift across the PFR directed to the inner divertor may play a role in the divertor electron density, particle flux, and heat flux asymmetries. The

This article is copyrighted as indicated in the article. Reuse of AIP content is subject to the terms at: http://scitation.aip.org/termsconditions. Downloaded to IP: 192.38.67.112 On: Thu, 25 Dec 2014 10:55:46

outboard enhanced target power asymmetries were observed by many tokamaks in LSN configuration, but there are very few reports about the divertor asymmetry in USN configuration. Detailed divertor asymmetry observations in LSN, DN, and USN configurations on EAST presented here may shed more light on these intriguing results, divertor asymmetry and particle transport in SOL.

In the post-GPI phase, the density, as well as the particle fluxes, as manifested by the ion saturation currents, increases evidently in UO divertor, the temperature $T_e$ increases near the strike point but reduces elsewhere, leading to an outboard enhanced peak heat flux asymmetry. As shown in Fig. 17, the $V_\theta$ of upper GPI in USN configuration is about 3 times as larger as that in LSN configuration, enhancing the effect of poloidal $E \times B$ drift in SOL which transports particle to UO divertor. The major difference between LSN and USN configurations is that the peak heat flux of the LO target decreases, but that of the UO target increases due to the gas injection. As mentioned in Sec. II, the intensity of gas puff for the upper GPI is much smaller than the lower GPI, therefore much more helium gas moves to LO divertor and cools there due to the short connection length between the lower GPI and the LO divertor in LSN configuration. Another important mechanism is the parallel flow in LFS SOL directed downwards which reduces the amount of helium gas into the UO divertor, especially for the helium injected by the lower GPI, which is demonstrated by Figs. 11 and 12: the maximum poloidal particle flux near separatrix in USN directed downwards is ~4 times larger than that in LSN configuration, and the integrated total poloidal particle flux in USN is ~3 times larger than that in LSN configuration in post-GPI phase. The modified Bohm boundary condition further reduces the helium transported to UO target. Consequently, the strong cooling effect is not observed in the UO divertor for USN in contrast to LSN. The density increases at the UI target mostly due to the increase of the plasma line averaged density.

### C. DN configuration

In the pre-GPI phase, the peak heat fluxes at the UI and UO targets are equal, and larger than that of the LO, and especially the LI targets. For Ohmic discharges, up-down peak heat flux asymmetry in LFS divertors favors the upper divertor in pre-GPI phase, in the same direction as ion $B \times \nabla B$ drift.

In the post-GPI phase, the temperature near separatrix at UO target decreases significantly while the density increases, leading to a little drop of peak heat flux, but the total deposition power at the outer targets exhibits a small increase, as shown in Fig. 5. The cooling effect at LO target is weaker than UO target. Consistent with the up-down asymmetry in pre-GPI phase, the UO target receives large part of particles and the plasma near the strike point is cooled. However, the poloidal particle flux at outer midplane is enhanced by gas puff and directed downwards, as shown in Fig. 11, but the integrated total poloidal particle flux is still much smaller than that in USN configuration. In addition, the poloidal velocity measured by GPI diagnostics during helium gas puff in DN configuration exhibits larger peak value and broad radial distribution than that in LSN and USN configuration, as shown in Fig. 17. Compared to outer midplane, the parallel flow velocity at the locations of GPI diagnostics decreases greatly because the PS flow will decrease towards zero near the X-point.[27] Since the poloidal $E \times B$ drift in SOL can be estimated from $V_\theta$ measured by GPI diagnostics, the poloidal $E \times B$ drift probably causes the up-down asymmetry in LFS in DN configuration.

As demonstrated by our experiment, the poloidal $E \times B$ drift in SOL does not always enhance the divertor particle flux in the direction of drift, while poloidal $E \times B$ drift directed away from divertor can increase the divertor density and particle flux by modified Bohm boundary condition.

## V. CONCLUSION

A series of experiments have been carried out to investigate the divertor asymmetry during helium gas puffing in various divertor configurations in EAST. The divertor temperature, density, and heat flux are measured by Langmuir probes, the radiated power is measured by a resistive bolometer and two XUV arrays, and the upstream parameters and parallel flow are measured by reciprocating probes at the outer midplane. The helium gas injected into the LFS plasma edge moves along the magnetic field line to the divertor region through friction and thermal forces after ionization. Both the plasma stored energy and radiated power increase ~10% after helium injection, indicating the amount of helium gas is not too much to cool the main plasma. In LSN configuration, a large portion of helium ions are transported to the LO divertor due to the parallel SOL flow which is enhanced by the in-vessel cryopump and the modified Bohm boundary condition. Therefore, significantly cooling effect is observed at the LO target due to a large increase of radiation, while the heat flux at LI target increases gradually presumably due to the poloidal $\mathbf{E} \times \mathbf{B}$ drift in SOL. In USN configuration, the density and heat flux at UO target increase significantly and the cooling effect is very weak, presumably due to that the smaller gas injection intensity of upper GPI compared to lower GPI and the reduction of parallel flow directed to UO target by modified Bohm boundary condition. In DN configuration, the LFS up-down asymmetry in both the pre-GPI and post-GPI phases are consistent with the poloidal $\mathbf{E} \times \mathbf{B}$ drift which is more important than that in LSN and USN configurations. Detailed divertor asymmetry observations in LSN, DN, and USN configurations on EAST presented here may shed more light on some intriguing issues, divertor asymmetry, and particle transport in SOL.

## ACKNOWLEDGMENTS

The authors would like to thank the EAST Team for their cooperation and kind help. This work was supported by the National Magnetic Confinement Fusion Research Program of China under Contract Nos. 2010GB104001, 2014GB106005, 2011GB107001, 2011GB101000, and 2013GB107003, and the National Natural Science Foundation of China under Grant Nos. 11275234, 10990212, and 11105177.

This article is copyrighted as indicated in the article. Reuse of AIP content is subject to the terms at: http://scitation.aip.org/termsconditions. Downloaded to IP: 192.38.67.112 On: Thu, 25 Dec 2014 10:55:46

[1]N. Asakura, H. Takenaga, S. Sakurai, G. D. Porter, T. D. Rognlien, M. E. Rensink, K. Shimizu, S. Higashijima, and H. Kubo, Nucl. Fusion **44**, 503 (2004).
[2]H. Takenaga, A. Sakasai, H. Kubo, N. Asakura, M. J. Schaffer, T. W. Petrie, M. A. Mahdavi, D. R. Baker, S. L. Allen, G. D. Porter, T. D. Rognlien, M. E. Rensink, D. P. Stotler, and C. F. F. Karney, Nucl. Fusion **41**, 1777 (2001).
[3]N. Asakura, H. Hosogane, S. TsujiIio, K. Itami, K. Shimizu, and M. Shimada, Nucl. Fusion **36**, 795 (1996).
[4]T. Eich, P. Andrew, A. Herrmann, W. Fundamenski, A. Loarte, and R. A. Pitts, Plasma Phys. Controlled Fusion **49**, 573 (2007).
[5]G. F. Matthews, S. K. Erents, W. Fundamenski, C. Ingesson, R. D. Monk, and V. Riccardo, J. Nucl. Mater. **290**, 668 (2001).
[6]A. V. Chankin, D. J. Campbell, S. Clement, S. J. Davies, L. D. Horton, J. Lingertat, A. Loarte, G. F. Matthews, R. D. Monk, R. Reichle, G. Saibene, M. Stamp, and P. C. Stangeby, Plasma Phys. Controlled Fusion **38**, 1579 (1996).
[7]A. W. Leonard, W. Suttrop, T. H. Osborne, T. E. Evans, D. N. Hill, A. Herrmann, C. J. Lasnier, D. N. Thomas, J. G. Watkins, W. P. West, M. Weinlich, and H. Zohm, J. Nucl. Mater. **241–243**, 628 (1997).
[8]A. Herrmann, W. Junker, K. Gunther, S. Bosch, M. Kaufmann, J. Neuhauser, G. Pautasso, T. Richter, and R. Schneider, Plasma Phys. Controlled Fusion **37**, 17 (1995).
[9]T. W. Petrie, C. M. Greenfield, R. J. Grobener, A. W. Hyatt, R. J. La Haye, A. W. Leonard, M. A. Mahdavi, T. H. Osborne, M. J. Schaffer, D. M. Thomas, W. P. West, S. L. Allen, M. E. Fenstermacher, C. J. Lasnier, G. D. Porter, N. S. Wolf, J. G. Watkins, and T. L. Rhodes, and DIII-D Team, J. Nucl. Mater. **290**, 935 (2001).
[10]M. W. Jakubowski, T. E. Evans, M. E. Fenstermacher, C. J. Lasnier, R. C. Wolf, L. R. Baylor, J. A. Boedo, K. H. Burrell, J. S. deGrassie, P. Gohil, S. Mordijck, R. Laengner, A. W. Leonard, R. A. Moyer, T. W. Petrie, C. C. Petty, R. I. Pinsker, T. L. Rhodes, M. J. Schaffer, O. Schmitz, P. B. Snyder, H. Stoschus, T. H. Osborne, D. M. Orlov, E. A. Unterberg, and J. G. Watkins, J. Nucl. Mater. **415**, S901 (2011).
[11]U. Wenzel, D. P. Coster, A. Kallenbach, H. Kastelewicz, M. Laux, H. Maier, R. Schneider, and ASDEX Upgrade Team, Nucl. Fusion **41**, 1695 (2001).
[12]V. A. Soukhanovskii, R. Maingi, A. L. Roquemore, J. Boedo, C. Bush, R. Kaita, H. W. Kugel, B. P. LeBlanc, S. F. Paul, G. D. Porter, N. S. Wolf, and NSTX Research Team, J. Nucl. Mater. **337**, 475 (2005).
[13]A. Huber, J. Rapp, P. Andrew, P. Coad, G. Corrigan, K. Erents, W. Fundamenski, L. C. Ingesson, S. Jachmich, A. Korotkov, G. F. Matthews, P. Mertens, V. Philipps, R. Pitts, B. Schweer, G. Sergienko, M. Stamp, and JET EFDA Contributors, J. Nucl. Mater. **337**, 241 (2005).
[14]W. Fundamenski, R. A. Pitts, G. F. Matthews, V. Riccardo, S. Sipila, and JET EFDA Contributors, Nucl. Fusion **45**, 950 (2005).
[15]P. C. Stangeby and A. V. Chankin, Nucl. Fusion **36**, 839 (1996).
[16]V. Rozhansky, P. Molchanov, I. Veselova, S. Voskoboynikov, A. Kirk, and D. Coster, Nucl. Fusion **52**, 103017 (2012).
[17]T. W. Petrie, G. D. Porter, N. H. Brooks, M. E. Fenstermacher, J. R. Ferron, M. Groth, A. W. Hyatt, R. J. L. Haye, C. J. Lasnier, A. W. Leonard, T. C. Luce, P. A. Politzer, M. E. Rensink, M. J. Schaffer, M. R. Wade, J. G. Watkins, and W. P. West, Nucl. Fusion **49**, 065013 (2009).
[18]T. D. Rognlien, G. D. Porter, and D. D. Ryutov, J. Nucl. Mater. **266–269**, 654 (1999).
[19]N. Asakura, H. Takenaga, S. Sakurai, H. Tamai, A. Sakasai, K. Shimizu, and G. D. Porter, Plasma Phys. Controlled Fusion **44**, 2101 (2002).
[20]S. K. Erents, R. A. Pitts, W. Fundamenski, J. P. Gunn, and G. F. Matthews, Plasma Phys. Controlled Fusion **46**, 1757 (2004).
[21]M. Tsalas, A. Herrmann, A. Kallenbach, H. W. Muller, J. Neuhauser, V. Rohde, N. Tsois, M. Wischmeier, and ASDEX Upgrade Team, Plasma Phys. Controlled Fusion **49**, 857 (2007).
[22]H. W. Muller, V. Bobkov, A. Herrmann, M. Maraschek, J. Neuhauser, V. Rohde, A. Schmid, and M. Tsalas, J. Nucl. Mater. **363**, 605 (2007).
[23]J. A. Boedo, R. Lehmer, R. A. Moyer, J. G. Watkins, G. D. Porter, T. E. Evans, A. W. Leonard, and M. J. Schaffer, J. Nucl. Mater. **266**, 783 (1999).
[24]B. LaBombard, J. W. Hughes, N. Smick, A. Graf, K. Marr, R. McDermott, M. Reinke, M. Greenwald, B. Lipschultz, J. L. Terry, D. G. Whyte, S. J. Zweben, and Alcator C-Mod Team, Phys. Plasmas **15**, 056106 (2008).
[25]J. A. Boedo, N. Crocker, L. Chousal, R. Hernandez, J. Chalfant, H. Kugel, P. Roney, J. Wertenbaker, and NSTX Team, Rev. Sci. Instrum. **80**, 123506 (2009).
[26]J. P. Gunn and V. Fuchs, Phys. Plasmas **14**, 032501 (2007).
[27]R. A. Pitts, J. Horacek, W. Fundamenski, O. E. Garcia, A. H. Nielsen, M. Wischmeier, V. Naulin, and J. J. Rasmussen, J. Nucl. Mater. **363**, 505 (2007).
[28]N. Asakura, S. Sakurai, M. Shimada, Y. Koide, N. Hosogane, and K. Itami, Phys. Rev. Lett. **84**, 3093 (2000).
[29]N. Asakura, J. Nucl. Mater. **363**, 41 (2007).
[30]G. S. Xu, B. N. Wan, H. Q. Wang, H. Y. Guo, H. L. Zhao, A. D. Liu, V. Naulin, P. H. Diamond, G. R. Tynan, M. Xu, R. Chen, M. Jiang, P. Liu, N. Yan, W. Zhang, L. Wang, S. C. Liu, and S. Y. Ding, Phys. Rev. Lett. **107**, 125001 (2011).
[31]Q. S. Hu, D. M. Yao, G. N. Luo, H. Xie, C. S. Xu, J. G. Li, and X. M. Wang, Fusion Eng. Des. **85**, 1508 (2010).
[32]T. F. Ming, W. Zhang, J. F. Chang, J. Wang, G. S. Xu, S. Ding, N. Yan, X. Gao, and H. Y. Guo, Fusion Eng. Des. **84**, 57 (2009).
[33]W. Zhang, J. F. Chang, B. N. Wan, G. S. Xu, C. J. Xiao, B. Li, C. S. Xu, N. Yan, L. Wang, S. C. Liu, M. Jiang, and P. Liu, Rev. Sci. Instrum. **81**, 113501 (2010).
[34]Y. M. Duan, L. Q. Hu, K. Y. Chen, W. Du, and L. Zhang, J. Nucl. Mater. **438**, S338 (2013).
[35]Y. M. Duan, L. Q. Hu, S. T. Mao, P. Xu, K. Y. Chen, S. Y. Lin, G. Q. Zhong, J. Z. Zhang, L. Zhang, and L. Wang, Plasma Sci. Technol. **13**, 546 (2011).
[36]S. C. Liu, L. M. Shao, S. J. Zweben, G. S. Xu, H. Y. Guo, B. Cao, H. Q. Wang, L. Wang, N. Yan, S. B. Xia, W. Zhang, R. Chen, L. Chen, S. Y. Ding, H. Xiong, Y. Zhao, B. N. Wan, X. Z. Gong, and X. Gao, Rev. Sci. Instrum. **83**, 123506 (2012).
[37]Y. M. Duan, L. Q. Hu, S. T. Mao, K. Y. Chen, S. Y. Lin, and EAST Diagnostics Team, Rev. Sci. Instrum. **83**, 093501 (2012).
[38]F. M. Wang, K. F. Gan, X. Z. Gong, and EAST Team, Plasma Sci. Technol. **15**, 225 (2013).
[39]C. S. Pitcher and P. C. Stangeby, Plasma Phys. Controlled Fusion **39**, 779 (1997).
[40]L. Wang, G. S. Xu, H. Y. Guo, R. Chen, S. Ding, K. F. Gan, X. Gao, X. Z. Gong, M. Jiang, P. Liu, S. C. Liu, G. N. Luo, T. F. Ming, B. N. Wan, D. S. Wang, F. M. Wang, H. Q. Wang, Z. W. Wu, N. Yan, L. Zhang, W. Zhang, X. J. Zhang, S. Z. Zhu, and EAST Team, Nucl. Fusion **52**, 063024 (2012).
[41]R. A. Pitts, P. Andrew, G. Arnoux, T. Eich, W. Fundamenski, A. Huber, C. Silva, D. Tskhakaya, and JET EFDA Contributors, Nucl. Fusion **47**, 1437 (2007).
[42]S. C. Liu, H. Y. Guo, G. S. Xu, X. Gao, S. Z. Zhu, H. Q. Wang, L. Wang, N. Yan, D. S. Wang, P. Liu, M. Jiang, W. Zhang, T. F. Ming, J. F. Chang, S. Y. Ding, H. Xiong, L. M. Shao, Z. W. Wu, G. N. Luo, and EAST Team, Phys. Plasmas **19**, 042505 (2012).
[43]N. Asakura, S. Sakurai, K. Itami, O. Naito, H. Takenaga, S. Higashijima, Y. Koide, Y. Sakamoto, H. Kubo, and G. D. Porter, J. Nucl. Mater. **313**, 820 (2003).
[44]S. J. Levinson, J. M. Beall, E. J. Powers, and R. D. Bengtson, Nucl. Fusion **24**, 527 (1984).
[45]J. M. Beall, Y. C. Kim, and E. J. Powers, J. Appl. Phys. **53**, 3933 (1982).
[46]G. D. Conway, C. Angioni, F. Ryter, P. Sauter, J. Vicente, and ASDEX Upgrade Team, Phys. Rev. Lett. **106**, 065001 (2011).
[47]G. S. Xu, V. Naulin, B. N. Wan, H. Y. Guo, W. Zhang, J. F. Chang, N. Yan, S. Y. Ding, L. Zhang, L. Wang, S. C. Liu, P. Liu, M. Jiang, H. Q. Wang, J. J. Rasmussen, A. H. Nielsen, C. J. Xiao, X. Gao, L. Q. Hu, S. Z. Zhu, Z. W. Wu, J. P. Qian, and X. Z. Gong, Plasma Sci. Technol. **13**, 397 (2011).
[48]P. C. Stangeby, *The Plasma Boundary of Magnetic Fusion Devices* (Institute of Physics Publishing, Bristol, 2000).
[49]L. Aho-Mantila, M. Wischmeier, K. Krieger, V. Rohde, A. Hakola, S. Potzel, A. Kirschner, D. Borodin, and ASDEX Upgrade Team, Nucl. Fusion **52**, 103007 (2012).
[50]J. L. Terry, S. J. Zweben, O. Grulke, M. J. Greenwald, and B. LaBombard, J. Nucl. Mater. **337**, 322 (2005).
[51]S. J. Zweben, J. L. Terry, M. Agostini, R. Hager, J. W. Hughes, J. R. Myra, D. C. Pace, and Alcator C-Mod Group, Plasma Phys. Controlled Fusion. **54**, 025008 (2012).
[52]R. Ding, A. Kirschner, M. Z. Tokar, M. Koltunov, D. Borodin, S. Brezinsek, A. Kreter, J. L. Chen, J. G. Li, and G. N. Luo, J. Nucl. Mater. **415**, S270 (2011).
[53]J. Neuhauser, W. Schneider, R. Wunderlich, K. Lackner, and K. Behringer, J. Nucl. Mater. **121**, 194 (1984).

This article is copyrighted as indicated in the article. Reuse of AIP content is subject to the terms at: http://scitation.aip.org/termsconditions. Downloaded to IP: 192.38.67.112 On: Thu, 25 Dec 2014 10:55:46